Supporting information: Artificial-intelligence-driven discovery of catalyst "genes" with application to CO_2 activation on semiconductor oxides

A. Mazheika[1,*], Y. Wang[1], R. Valero[2], F. Viñes,[2] F. Illas[2], L. M. Ghiringhelli[1], S. V. Levchenko[3,1,*],
M. Scheffler[1]

[1]Fritz-Haber-Institut der Max-Planck-Gesellschaft, 14195 Berlin-Dahlem, Germany
[2]Departament de Ciència de Materials i Química Física and
Institut de Química Teòrica i Computacional (IQTCUB),
Universitat de Barcelona, c/ Martí i Franquès 1, Barcelona 08028, Spain
[3]Skolkovo Institute of Science and Technology, Skolkovo Innovation Center, 3 Nobel Street,
143026 Moscow, Russia

*corresponding authors: alex.mazheika@gmail.com, mazheika@fhi-berlin.mpg.de; levchenko@fhi-berlin.mpg.de

Ab initio methodology

All *ab initio* calculations were performed with the all-electron full-potential electronic structure FHI-aims code package[1] using density-functional theory (DFT) and numerical atom-centered basis functions. The standard 'tight' settings (grids and basis functions) were employed[1], which deliver the adsorption energies with basis-set superposition errors below 0.07 eV per adsorbed molecule. The exchange-correlation (XC) functional approximation was chosen based on a comparison to available experimental and high-level theoretical data on CO_2 adsorption energy (see below). PBE[2] and PBEsol[3] functionals with and without Tkatchenko-Scheffler (TS) pairwise dispersion-correction method[4] were tested. LDA[5] and RPBE[6] have been previously shown to give large errors for adsorption of CO_2[7,8]. All systems were treated as spin non-polarized. The bulk lattice vectors were calculated with the same exchange-correlation functional as the surface and the adsorbed molecule properties. The *k*-points for the bulk calculations were converged with respect to lattice vectors. The slabs were symmetric, and all atoms therein were allowed to relax. We did not constrain any side of a slab in order to have the same surface geometry on both sides, which is important for calculation of surface primary features. The slab thickness was also tested, and it was set to about 11 Å or larger in most cases, based on the convergence of the surface energy (within 5 meV/Å^2) and the work function (within 10 meV) with respect to the thickness. For the surface supercells the *k*-grids were scaled from corresponding bulk grids. The lattice constants were obtained from the relaxed bulk unit cells. The initial geometries of adsorbed CO_2 before full atomic relaxation were obtained by placing the CO_2 molecule at different possible adsorption sites (metal and O sites, top, bridge, and hollow sites) and in different orientations (C down, O down) on one side of the slab. The size of the surface supercells was set based on test calculations, so that the interaction between the periodic images of the adsorbed CO_2 was below 0.1 eV. The resulting distance between the images of the C atom was about 8 Å. The adsorption of CO_2 has been considered only on one side of the slab, and a dipole correction[9] was included to prevent spurious electrostatic interactions. The lattice vector along the direction parallel to the vacuum gap was 200 Å. All atoms in the systems have been allowed to relax until the maximum remaining force fell below 10^{-2} eV/Å.

There are few experimental data available for CO_2 adsorption at clean monocrystalline surfaces without impurities: at CaO (001)[10] and at ZnO (10-10)[11,12]. We compared the calculated adsorption energies (E_{ads}) to the microcalorimetry and temperature programmed desorption (TPD) data. The adsorption energies were calculated as the difference between total energies of the slab with the adsorbed molecule, clean surface slab, and a free gas-phase CO_2 molecule. The calculations of the surfaces were performed with symmetric 5-atomic layer slabs for CaO (001) and 4 double-layer slab for ZnO (10-10). 8×8×8 and 10×10×6 *k*-point grids were used for cubic CaO and hexagonal ZnO bulk unit cells, respectively. Surface unit cells were (2×2) for CaO (001), for ZnO (10-10) we considered two cells – (1×1) and (1×2).

The results for CaO (001) and ZnO (10-10) are shown in Table S1. In the case of CaO the PBE adsorption energy is the closest to the experimentally observed value both from TPD and microcalorimetry, whereas PBEsol and PBEsol+TS values are closer to the one obtained with CCSD(T) using an embedded cluster model[10]. The inconsistency of the high-level theoretical and the experimental results was explained[10] by the formation of agglomerates of adsorbed CO_2 molecules even in ultrahigh vacuum. Relative to CCSD(T), PBEsol+TS performs better.

Table S1. The experimental and theoretical energies of adsorption (in eV) of CO_2 at CaO (001) and ZnO (10-10) surfaces.

method	CaO (001)	ZnO (10-10)		MgO (001)
		(1×1) structure	(1×2) structure	
PBE	-1.32	-0.45	-0.67	-0.34
PBE+TS	-1.47	-0.79	-0.96	-0.53
PBEsol	-1.60	-0.84	-1.04	-0.63
PBEsol+TS	-1.75	-1.00	-1.19	-0.79
TPD	-1.24 – -1.45 [10]	-0.55 [11]	-0.90 [11,12]	-0.41 [14]

microcalorimetry	~ -1.30 [10]	-0.72 [12]	-1.12 [12]	-
high-level calculations	-1.91 ± 0.10[a] [10]	-	-	-0.64[b] [15]

[a]CCSD(T); [b]HSE(0.3)+vdW

In the case of ZnO (10-10) the experimental data have been obtained for two adsorption coverages: 100% [(1×1) structure] and 50% [(1×2) structure]. In contrast to CaO, TPD and microcalorimetry values differ by about 0.2 eV (Table S1). Taking into account that the calculated thermo-desorption energies depend on the chosen kinetic model as well as on the pre-exponential factor, we consider the microcalorimetry results as more accurate. The PBEsol adsorption energies match both measured values with the best accuracy (~0.1 eV). PBEsol+TS slightly overestimates the adsorption energies. This is not unexpected, since PBEsol functional behaves similarly to LDA for interatomic interactions at the middle-range distances, so that inclusion of additional vdW-correction leads to overestimation of binding energies. In addition, the TS scheme based on non-iterative Hirshfeld partitioning of the electron density was found to fail in predicting adsorption energies for some ionic systems, due to inaccurate description of polarizabilities[13].

We also compare the GGA CO_2 adsorption energies for MgO (001) surface with hybrid HSE(0.3)+vdW functional results[15], where HSE(0.3)+vdW is the HSE functional with 30% fraction of exact exchange plus the many-body dispersion correction[16]. This functional was shown to yield CO_2 adsorption energies very close to CCSD(T) for embedded clusters[15], and the adsorption energy was found to be -0.64 eV. The closest value was obtained with the PBEsol functional (-0.63 eV). Thus, PBEsol compares favorably to both experiment and higher-level calculations. In addition to the above-mentioned systems, two more systems were tested: CO_2 adsorption on BaO-terminated $BaTiO_3$ (001) and on $CaZrO_3$ (101) surfaces. In general, we find that *relative differences* in adsorption energy between different XC approximations are weakly dependent on the material and surface termination (Figure S1, left).

In addition to adsorption energies, another important parameter of CO_2 adsorption is the OCO angle, which is 180º in the neutral gas-phase molecule and close to 120º (as in a gas-phase CO_3^{2-} ion) in adsorbed systems. As there are no precise experimental data like in the case of adsorption energies, here we rely on a weak sensitivity of the OCO angle to XC functional approximations. PBE, PBE+TS, and PBEsol provide very close OCO-angles for all tested systems (Figure S1, right). The largest difference was observed in MgO (001) case where PBE+TS value is larger than PBE and PBEsol by 1.0°. In all other cases such deviation was 0.4 degree on average.

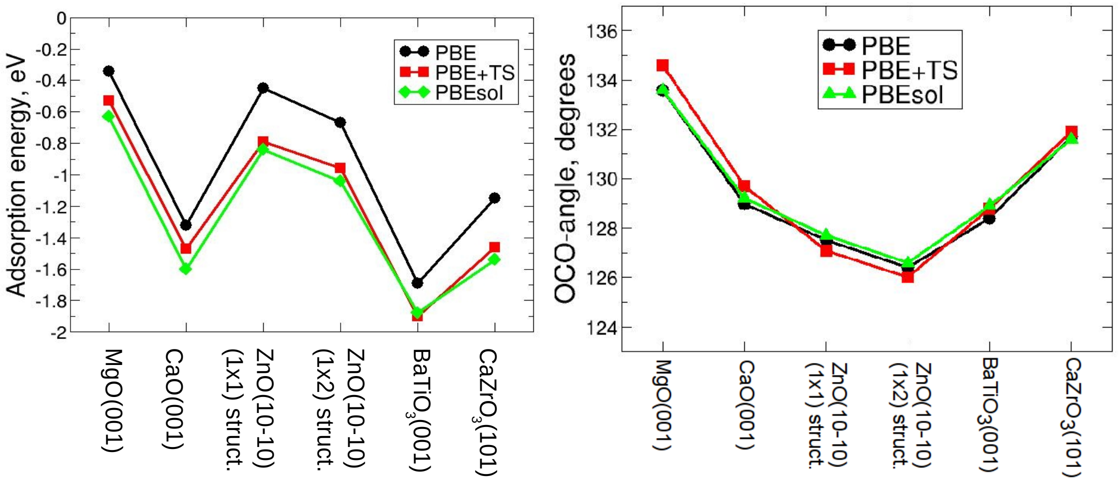

Figure S1. The adsorption energies (left) and OCO-angles (right) of adsorbed CO_2 for different surfaces and XC functionals.

Summarizing the test results and taking into account that PBEsol provides a very good agreement between calculated and experimental bulk lattice constants for ionic solids[3], we conclude that PBEsol is the best choice for our study. This result may be explained by the accuracy in prediction of lattice parameters in PBEsol[17] that results in a correct distribution of electronic density on surfaces.

Studied materials and surface terminations

In the current study we have focused on semiconductor (or insulating) oxide materials. Furthermore, we do not consider defects (*e.g.*, oxygen vacancies) and charge-carrier doping, which can significantly modify surface chemical properties. Despite these constraints, the selected materials class includes a large number of compounds (binary, ternary, and more complex oxides). Metallic oxides and defects on surfaces will be the object of the next study. In general, three groups of oxides have been considered: $A^{2+}B^{4+}O_3$, $A^{1+}B^{5+}O_3$, $A^{3+}B^{3+}O_3$ and all the binary oxides AO, BO_2, A_2O_3, A_2O, B_2O_3. For each oxide material we have considered a set of low-index surfaces with maximal Miller index up to 2. We mainly considered non-polar surfaces. For several included polar surfaces, reconstructions that compensate surface charge assuming formal charges of the ions were considered. All surfaces were insulating (with a non-vanishing gap between the highest occupied and lowest unoccupied states). In the cases when oxides have polymorphs (TiO_2, $MgGeO_3$ etc.) they were also included. The full list of materials and surface terminations is shown in Table S2. In general, 71 materials have been calculated with 141 surfaces including different terminations. Considering all non-equivalent adsorption sites on these surfaces, the total number of calculated unique CO_2 adsorption geometries is 255. All data, including initial and final geometries, and the computed properties, are available in the NOMAD database[16].

Table S2. Oxide materials, surface terminations, and the number of unique adsorption sites per termination.

material	surfaces	number of unique sites per surface
$MgSiO_3$	(001) MgO-term.	1
$MgTiO_3$	(001) (012)	1 2
$MgGeO_3$ hexagon.	(001) (012)	1 2
$MgGeO_3$ tetragon.	(001) MgO-term. (001) GeO_2-term.	1 1
$MgSnO_3$	(100)	2
$CaSiO_3$	(001) CaO-term. (001) SiO_2-term. (110) CaO-term. (110) SiO_2-term.	1 1 1 1
$CaTiO_3$	(010) CaO-term. (101) CaO-term. (100) TiO_2-term.	1 1 1
$CaGeO_3$	(001) CaO-term. (001) GeO_2-term. (110) CaO-term. (110) GeO_2-term.	1 2 1 2
$CaZrO_3$	(010) CaO-term. (101) CaO-term. (101) ZrO_2-term.	1 2 1
$CaSnO_3$	(001) SnO_2-term. (110) CaO-term. (110) SnO_2-term.	1 2 1
$SrSiO_3$	(001) SrO-term.	1
$SrTiO_3$	(001) SrO-term. (001) TiO_2-term.	1 1
$SrGeO_3$	(100) SrO-term. (100) TiO_2-term.	1 1
$SrZrO_3$	(001) ZrO_2-term. (110) SrO-term.	1 2
$SrSnO_3$	(001) SrO-term. (001) SnO_2-term. (110) SrO-term. (110) SnO_2-term.	1 1 1 1
$BaSiO_3$	(100) (101)	2 1
$BaTiO_3$	(001) BaO-term. (001) TiO_2-term.	1 1
$BaGeO_3$	(001) BaO-term.	1
$BaZrO_3$	(001) ZrO_2-term. (110) BaO-term.	1 1

$BaSnO_3$	(001) BaO-term. (001) SnO_2-term.	1 1
MgO	(001) (110) (111) octopolar O-term.	1 1 1
CaO	(001) (110) (111) octopolar O-term.	1 1 1
SrO	(001) (110) (111) octopolar O-term.	1 1 1
BaO	(001) (110) (111) octopolar O-term.	1 1 1
SiO_2	(001)	2
TiO_2 anatase	(101) (001)	2 1
TiO_2 rutile	(100) (110)	1 2
GeO_2	(100) (110)	1 2
ZrO_2	(001) (011) (111)	2 4 3
SnO_2	(100) (110)	1 2
ZnO	(10-10)	1
$LiNbO_3$	(100)	1
$NaNbO_3$ tetragon.	(010) (110)	2 1
$NaNbO_3$ P bcm	(100)	1
$KNbO_3$ tetragon.	(010) (110)	1 2
$RbNbO_3$ P1	(111)	2
$CsNbO_3$	(010) (100)	2 1
$LiVO_3$ orthogon.	(110)	2
$LiVO_3$ P bcm	(100)	1
$NaVO_3$	(010) (110)	1 1
KVO_3 orthogon.	(010)	1
$RbVO_3$ tetragon.	(010) (110)	1 1
$RbVO_3$ P bcm	(100)	1
$CsVO_3$ tetragon.	(010) (110)	1 1
$LiSbO_3$ tetragon.	(010)	1
$LiSbO_3$ P bcm	(100)	1
$NaSbO_3$ tetragon.	(010)	1

$NaSbO_3$ P bcm	(100)	2
$KSbO_3$ tetragon.	(110)	2
Na_2O	(011) (111)	1 1
$GaAlO_3$	(100)	2
$InAlO_3$ hexagon.	(110)	2
$InAlO_3$ orthorh.	(010) (110) (121)	3 4 3
$GaInO_3$	(100) (110) (120)	2 5 6
$ScAlO_3$	(010) (100) (110) (121)	1 2 2 6
$ScGaO_3$	(010) (110)	3 5
$ScInO_3$	(100) (110) In_2O_3-term. (110) $ScInO_3$-term. (121)	5 5 5 6
$YScO_3$	(100)	1
$LaScO_3$	(100)	1
$YInO_3$	(100) (110)	2 2
$YAlO_3$	(011) (100)	2 1
$LaYO_3$	(001)	2
$YGaO_3$	(100) (110)	2 2
$LaAlO_3$	(110)	2
$LaGaO_3$	(100) (110)	1 1
$LaInO_3$	(100)	1
Al_2O_3	(001) (012)	1 1
Ga_2O_3	(110) (212)	3 7
Sc_2O_3	(001) (110) (111)	3 5 5
In_2O_3	(001) (110) (111)	1 5 4
La_2O_3	(100) (110) (120) (201)	2 2 3 2

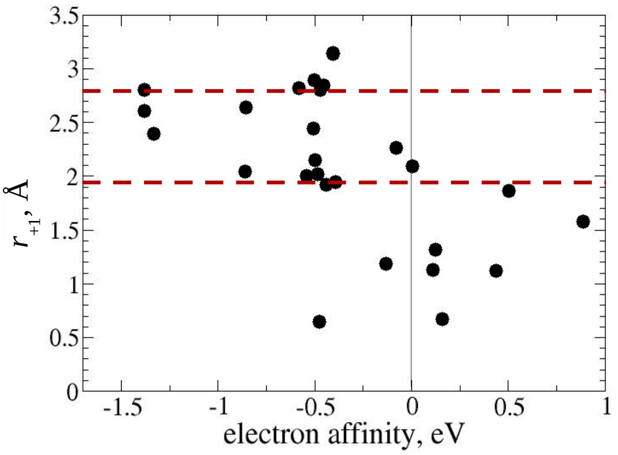

Figure S2. The dependence of LUMO radii (r_{+1}) on electron affinities. Red dashed lines show isovalues r_{+1} = 1.94 Å and 2.80 Å.

Table S3. The full list of used primary features calculated with PBEsol.

symbol	meaning
$IP_{\mathrm{min/max}}$, IP_{O}	ionization potential, minimal and maximal in the pair of atoms *A* and *B*, and for O; calculated as E_{atom} - E_{cation}
$EA_{min/max}$, EA_{O}	electron affinity, minimal and maximal in the pair of atoms *A* and *B*, and for O; calculated as E_{anion} - E_{atom}
$EN_{\mathrm{min/max}}$, EN_{O}	Mulliken electronegativity, minimal and maximal in the pair of atoms *A* and *B*, and for O
r_{HOMO}, r_{+1}, r_{-1}	maximum value of radial wave functions of the non-spin polarized spherically symmetric atom for HOMO, LUMO and HOMO-1
Δ	band gap of the whole surface slab
E_{form}	surface formation energy
VBM	valence-band maximum with respect to vacuum level
W	work function (*W* = -*VBM*)
q_{O}	Hirshfeld charge of O-atom
q_{min}, q_{max}	minimal and maximal Hirshfeld charges of cations in the pair *A* and *B*, calculated as an average for all surface cations of a given type
$\varphi_{1.4}$, $\varphi_{2.6}$, $\varphi_{1.4}$ - $\varphi_{2.6}$	electrostatic potentials above O-atom at 1.4 and 2.6 Å and their difference. 1.4 Å corresponds to the average length of the bond between C and surface O, 2.6 Å is the minimal distance from surface O to C-atom of physisorbed carbon-dioxide molecule as observed from our calculations
α_{O}, C_6^{O}	polarizability and C_6-coefficient for O-atom obtained from many-body dispersion scheme [16]
α_{min}, α_{max}, C_6^{min}, C_6^{max}	polarizability and C_6-coefficient for cations, minimal and maximal in the pair *A* and *B*, calculated as an average for all surface cations of a given type

Q_5, Q_6	local-order parameter with l = 5 or 6
d_1, d_2, d_3	distances from surface O-atom to the first-, second-, and third-nearest cations
BV	bond-valence value of O-atom
PC	weighted O 2p-band center
c_{min}, c_{max}	first moment for PDOS of cation within valence-band, minimal and maximal in the pair A and B, calculated as an average for all surface cations of a given type
wid	square-root of the second moment of O 2p-band
wid_{min}, wid_{max}	square-root of the second moment for PDOS of cations within valence-band, minimal and maximal in the pair A and B, calculated as an average for all surface cations of a given type
$skew$	skewness of O 2p-band PDOS
$kurt$	kurtosis of O 2p-band PDOS
CBm	conduction band minimum
L_{min}, L_{max}	energy of lowest unoccupied state of cation, minimal and maximal in the pair A and B, calculated as an average for all surface cations of a given type
M	energy at which the O 2p-band PDOS is maximal
U	eigenstate with least negative value in O 2p-band

Table S4. Top subgroups obtained by minimization of OCO-angle with/out energy constraint and corresponding distributions of samples according to adsorption energies, OCO-angles, and C-O bond distances.

cutoff	size	selector
without adsorption energy constraint		
123	9	q_O>=-0.39, Q_5<=0.81, Δ>=1.675, PC>-6.61, q_{min}<=0.58
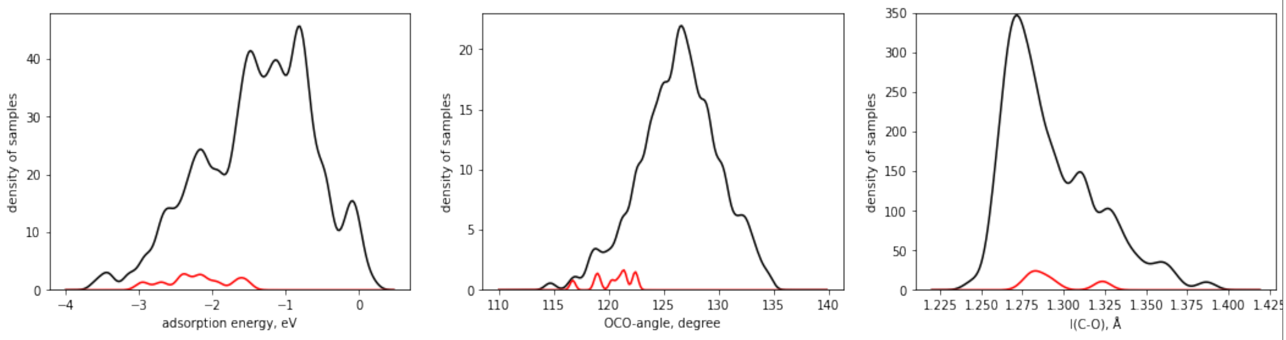		
124	14	L_{min}>-1.76, Q_5>=0.69, α_{max}>100.4, c_{max}<=-6.00, α_O<=1.63

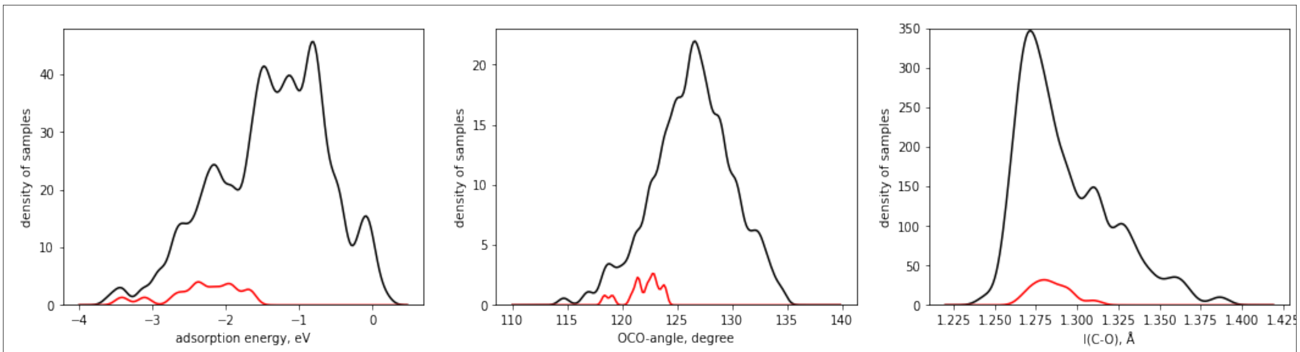		
126	19	$L_{max}>-2.70$, $IP_{max}\geq-6.05$, $\alpha_{max}\leq184.5$, $\Delta\varphi>1.33$, $q_{max}\leq0.59$, $wid\leq1.59$, $wid\geq0.58$
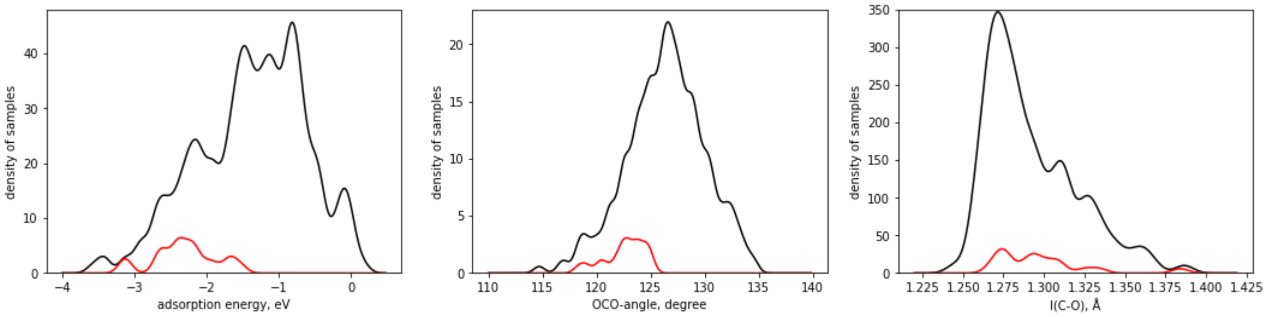		
128	44	$\mathrm{EA}_{\mathrm{max}}>=-0.425$, $\mathrm{Q}_6>=0.51$, $\alpha_{\mathrm{max}}>=50.4$, $\Delta\varphi>=1.00$, $\mathrm{q}_{\mathrm{min}}<=0.49$
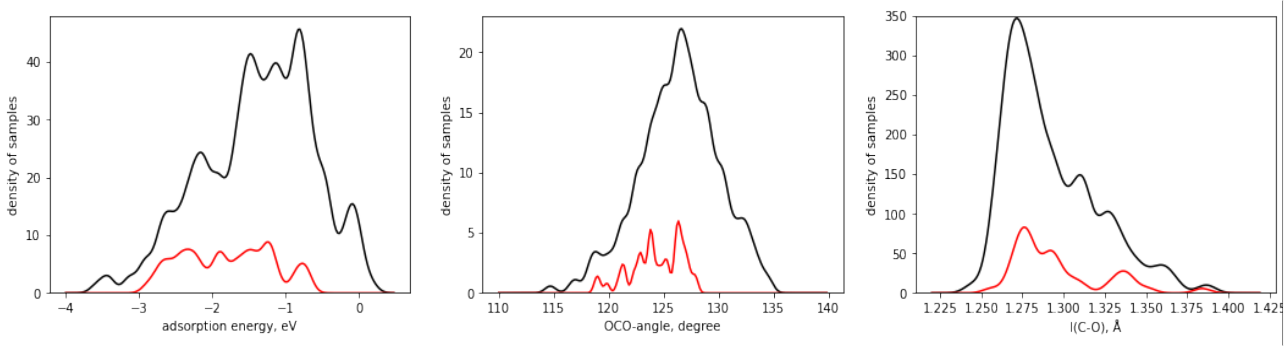		
130	77	$\mathrm{L}_{\mathrm{max}}>=-5.23$, $\mathrm{EA}_{\mathrm{max}}<=0.16$, $\mathrm{d}_1>=1.82$, $\mathrm{d}_2>2.10$
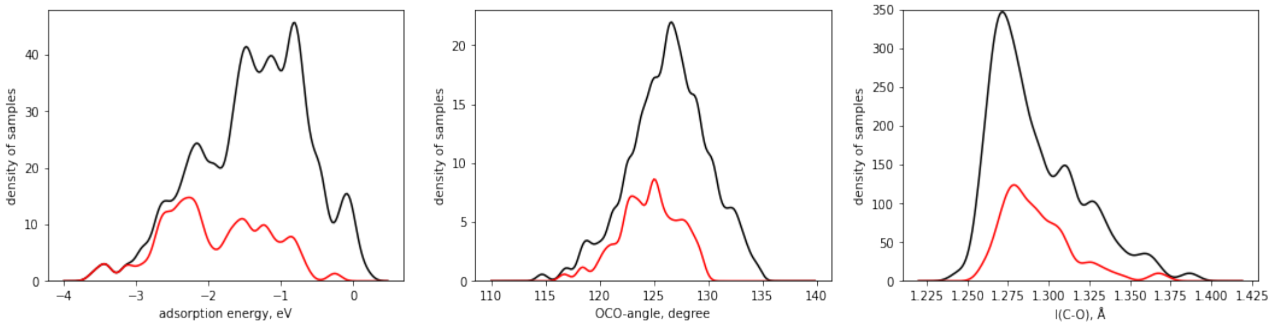		
132	139	$\mathrm{IP}_{\mathrm{max}}>=-6.99$, $\mathrm{q}_{\mathrm{O}}<=-0.32$, $\mathrm{C}_6^{\mathrm{O}}>=10.36$

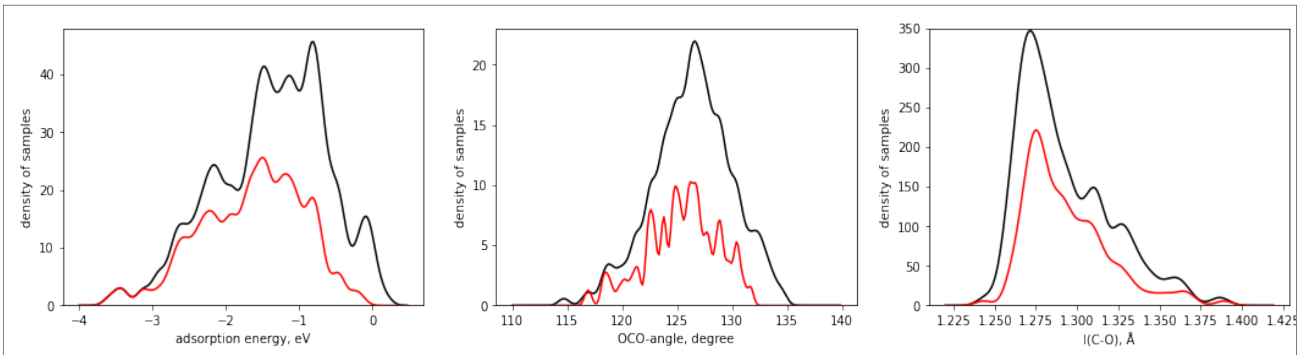

with adsorption energy constraint

123	8	Q_6<0.66, c_{max}>=-9.80, d_2>=2.00, M<=-4.12, wid_{min}>1.52

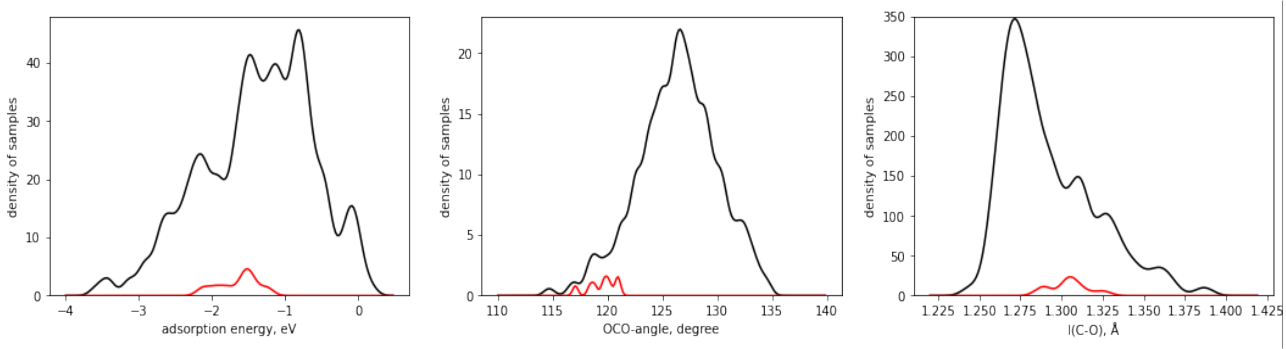

124	10	q_O<=-0.32, Q_6<0.66, Q_6>=0.57, Δφ>=0.60, r_{-1}^{max}<=1.65, wid>=1.24

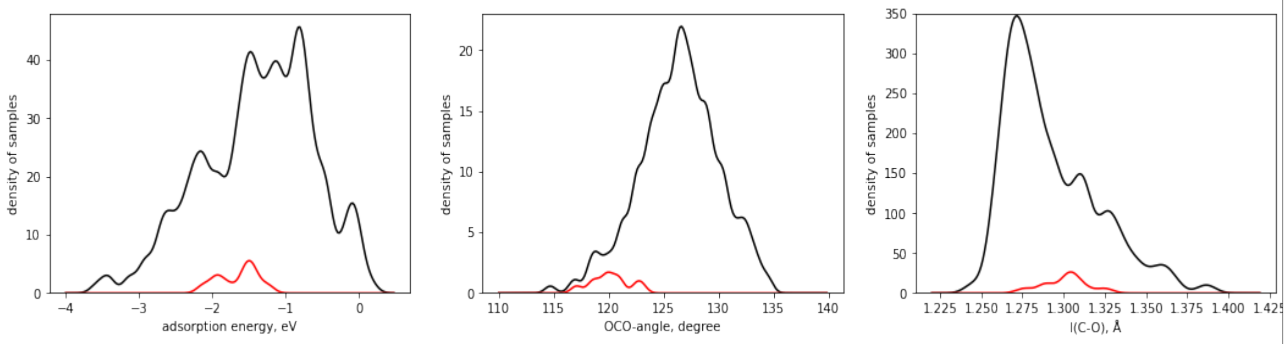

126	15	L_{min}≥-5.1085, $φ_{2.6}$≤0.3033, Δφ≤1.0622, d_1≥1.82, d_2≥2.005, r_{+1}^{max}>2.83

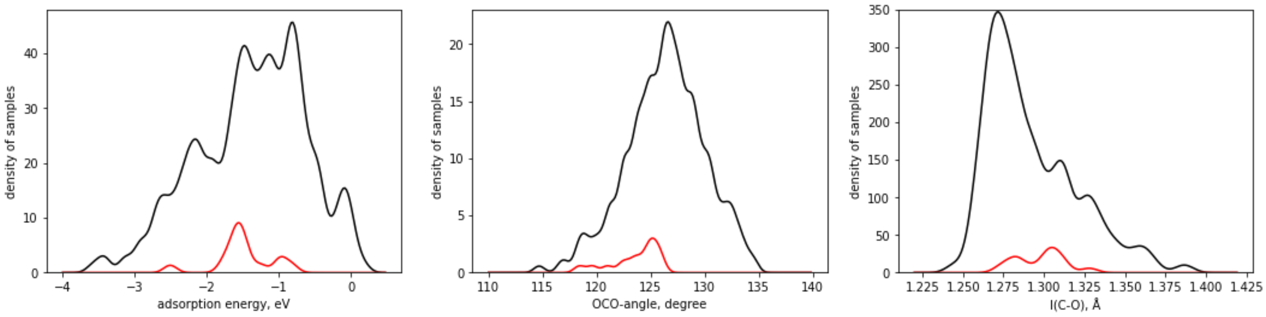

128	30	C_6^{min}>=369.5, L_{max}>=-4.73, Q_5<=0.83, Δφ>=0.60, $r_{+1,max}$>=2.80, C_6^O<=12.10

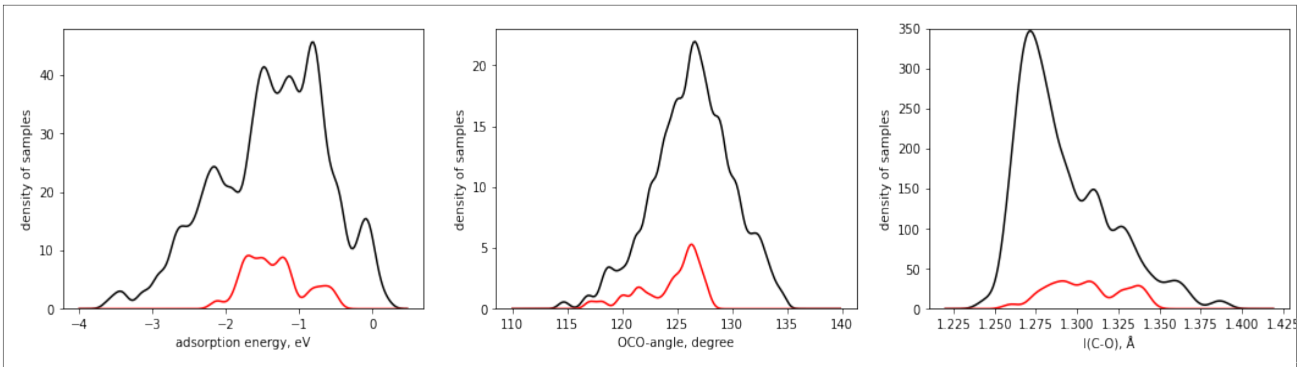

130	40	$\varphi_{2.6}$>=-0.15, $\Delta\varphi$>=0.73, d_1<=2.01, d_2>=1.96, d_3>=2.025, q_{min}<=0.49, r_{+1}^{min}>=1.94

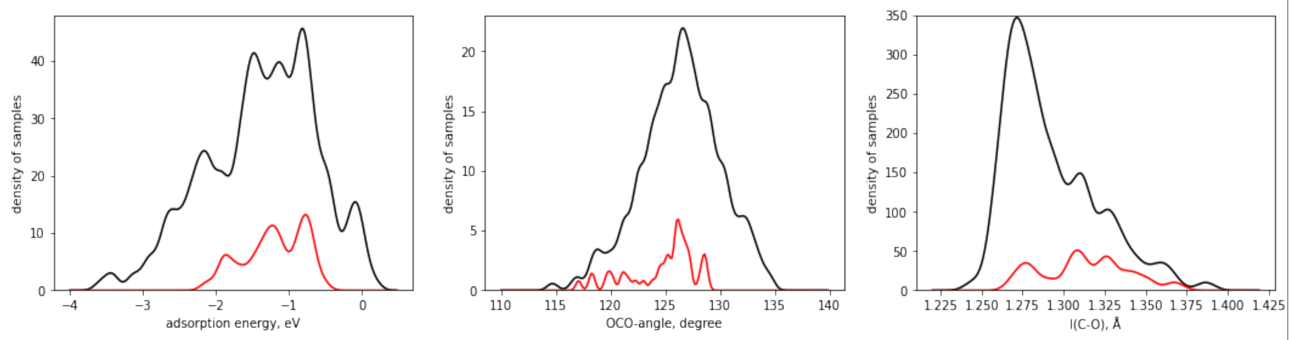

132	58	q_O≤-0.3386, M≤-6.292, $kurt$≥2.1035, IP_{max}≥-6.2085, r_{HOMO}^{min}≤1.407

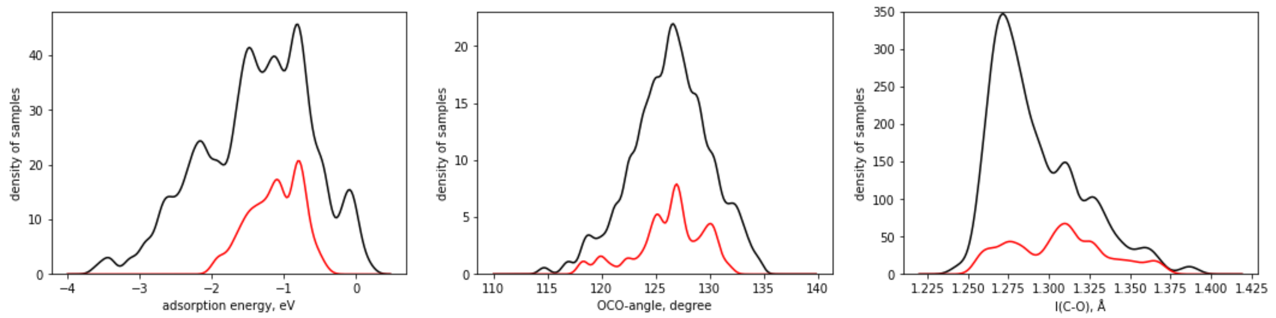

Table S5. Top subgroups obtained by maximization of *l*(C-O)-bond with/out energy constraint and corresponding distributions of samples according to adsorption energies, OCO-angles, and C-O bond distances.

cutoff	size	selector
without adsorption energy constraint		
1.26	121	C_6^{min}>=343.5, $\varphi_{2.6}$<=0.66, Q_5<=0.83, M>=-8.05

<table>
<tr><td colspan="3">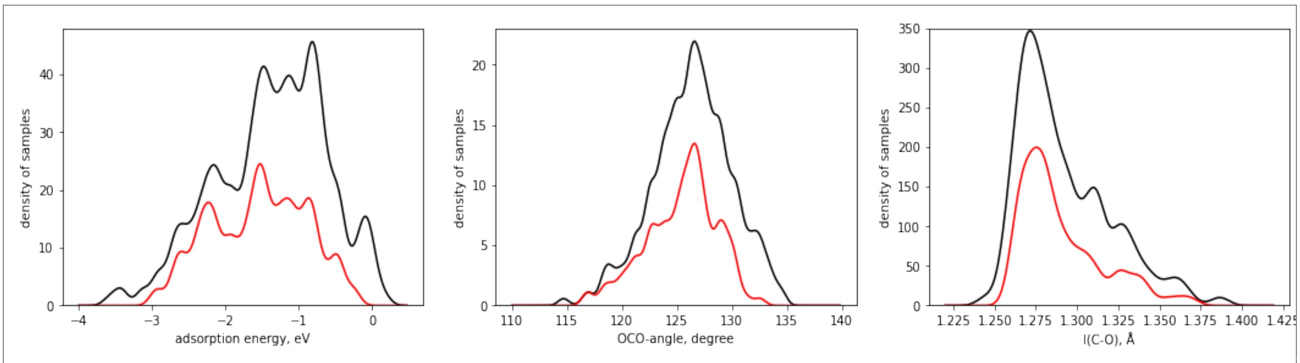
</td></tr>
<tr><td>1.28</td><td>38</td><td>EA_{max}<=0.005, d_2>2.22, M<=-4.12</td></tr>
<tr><td colspan="3">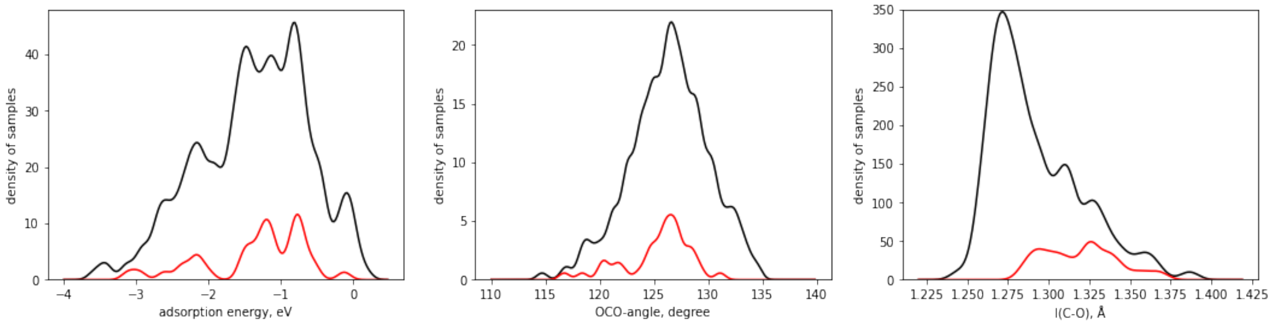
</td></tr>
<tr><td>1.30</td><td>27</td><td>kurt>=2.10, d_2>2.14, U<=-5.34, q_{min}<0.48</td></tr>
<tr><td colspan="3">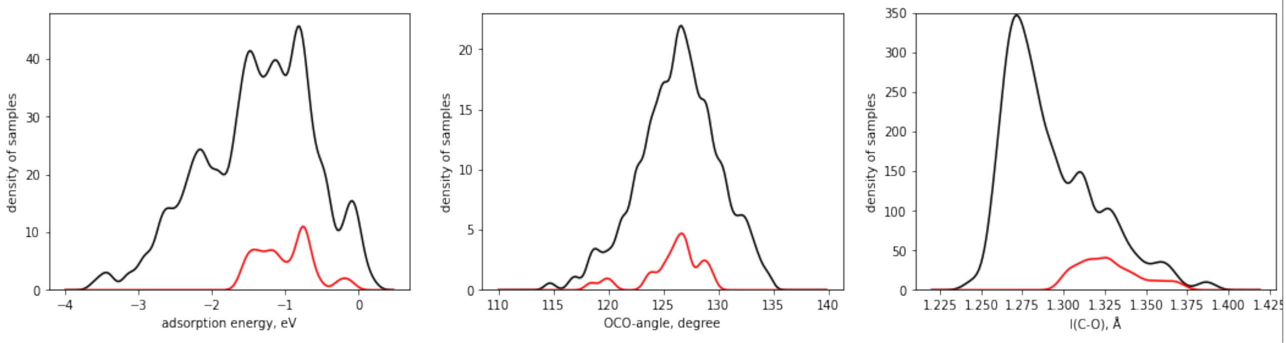
</td></tr>
<tr><td colspan="3"></td></tr>
<tr><td colspan="3">with adsorption energy constraint</td></tr>
<tr><td>1.26</td><td>56</td><td>CBM>=-5.17, Δφ<=1.13, <i>PC</i>>=-8.62, d_3<=2.48, M<=-6.06</td></tr>
<tr><td colspan="3">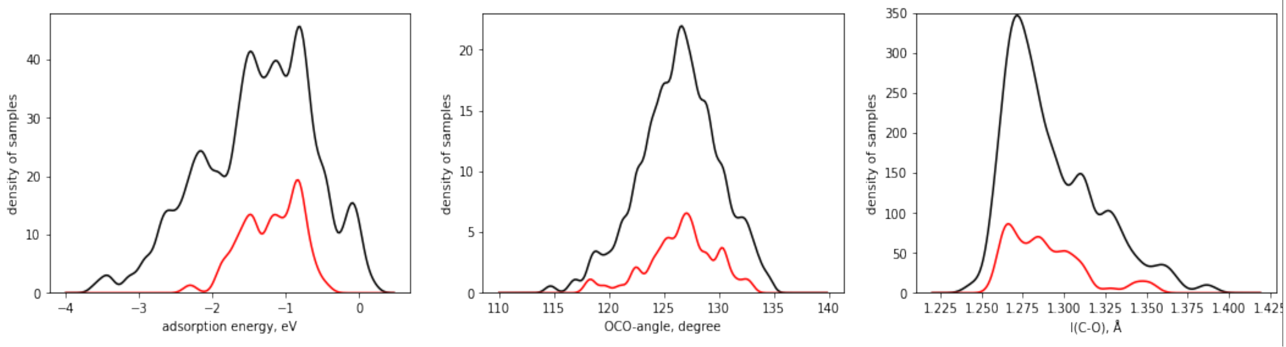
</td></tr>
<tr><td>1.28</td><td>30</td><td>W>=5.1, d_2>2.14, q_{min}<0.48</td></tr>
</table>

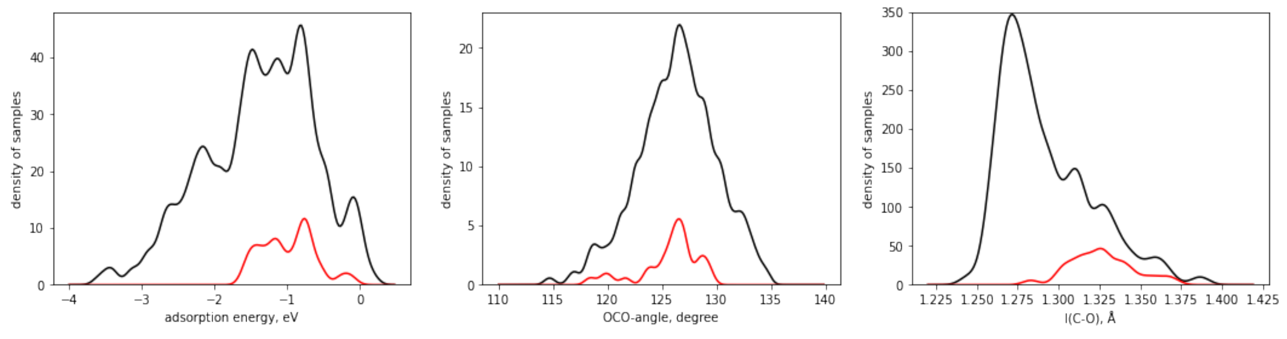

1.30	27	EA_{max}<=0.005, EN_{min}<=-3.19, kurt>=2.51, d_2>2.14, q_{min}<0.48

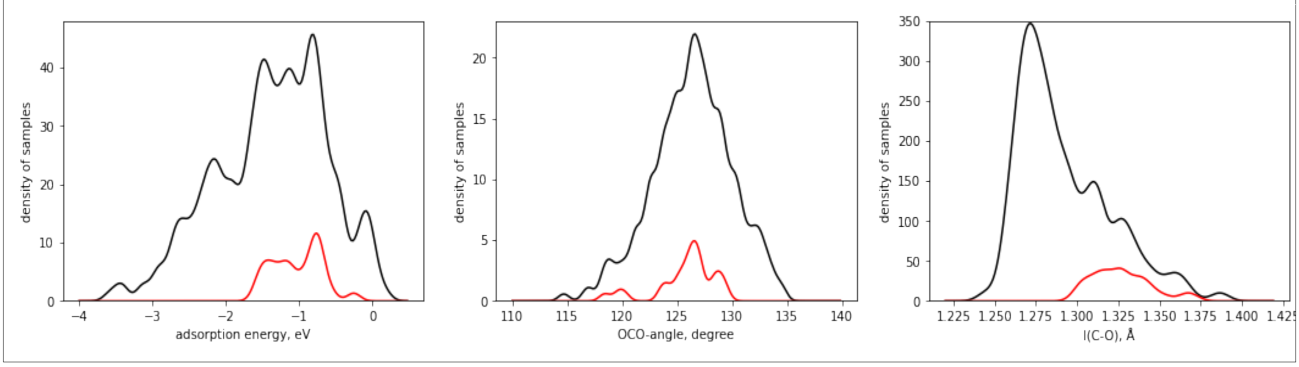

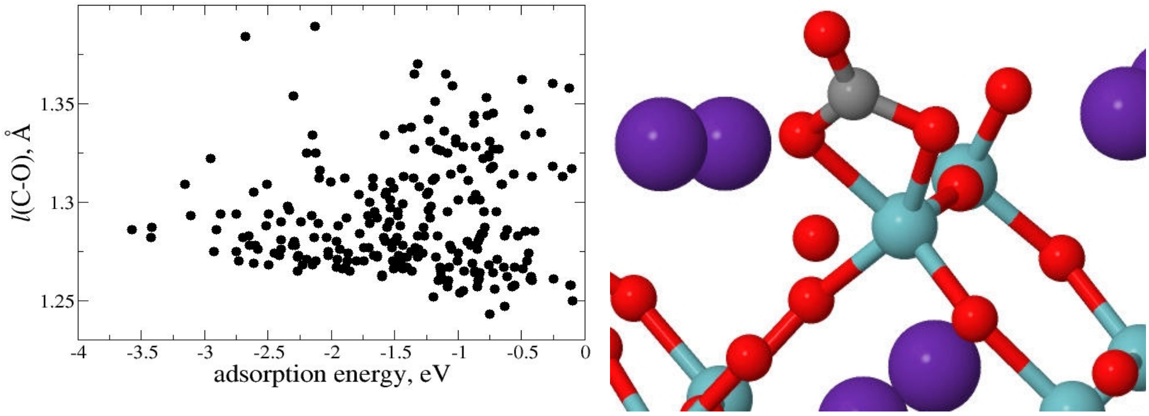

Figure S3. (left) The dependence of CO_2 adsorption energy on C-O bond length *l*(C-O). (right) Typical CO_2 adsorption structure from the subgroup with larger *l*(C-O). Color scheme: gray C, red O, cyan Nb, violet Rb.

Decision tree regression models obtained for *l*(C-O).

We have done a comparison of found SGD subgroups with DTR performance for *l*(C-O). Two cost functions were used in DTR – mean absolute error (MAE) and mean squared error (MSE), and the patterns with largest average *l*(C-O) values in each obtained tree were analyzed. We did not take into account the Sabatier principle explicitly in DTR, since there exists no standard decision tree algorithm wrapping regression and classification simultaneously. Thus, we do not consider DTR for OCO-angle.

The leave-one-out cross validation was used for the search of the optimal set of hyperparameters – minimal size of a leaf and maximum depth of the tree. The search was done on a grid at first for the minimal size of a leaf, then for selected local and global minima for maximum depth of the tree with fixed minimal sizes. The most optimal sets of hyperparameters {min. size, max. depth} are {27, 4} for *l*(C-O) DTR model with MSE cost function and {60, 2} for *l*(C-O) DTR model with MAE (Figure S4). With these sets of hyperparameters the regression trees shown in Figure S5 were obtained.

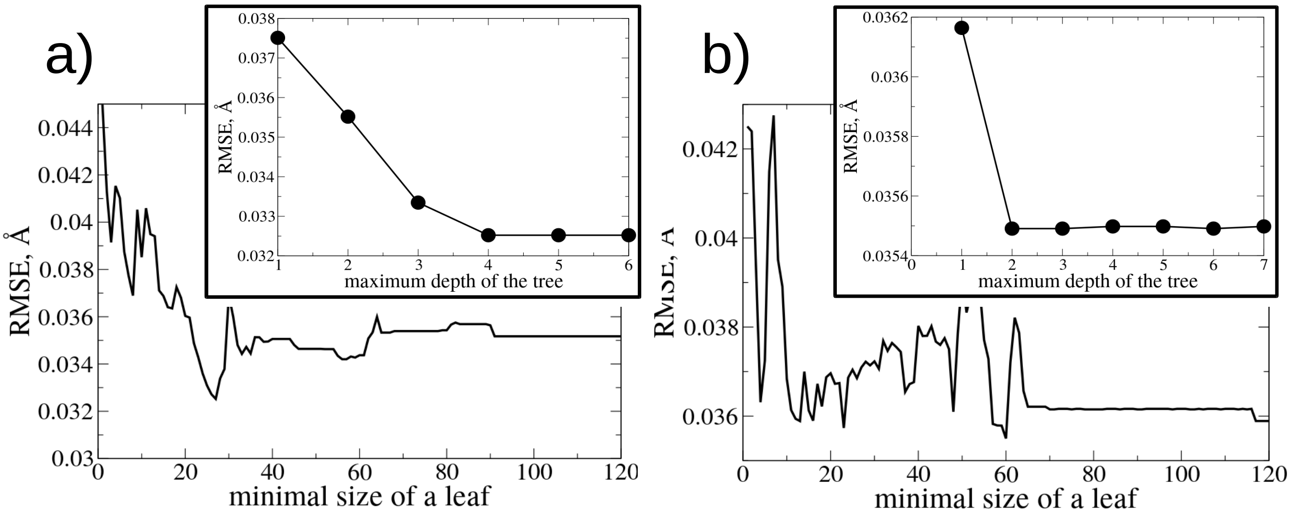

Figure S4. The results of leave-one-out cross-validation for tree regression models with respect to the minimal size of a leaf and next the maximum depth of the tree (insets): a) *l*(C-O) as the target with MSE as the cost function; b) *l*(C-O) as the target with MAE as the cost function.

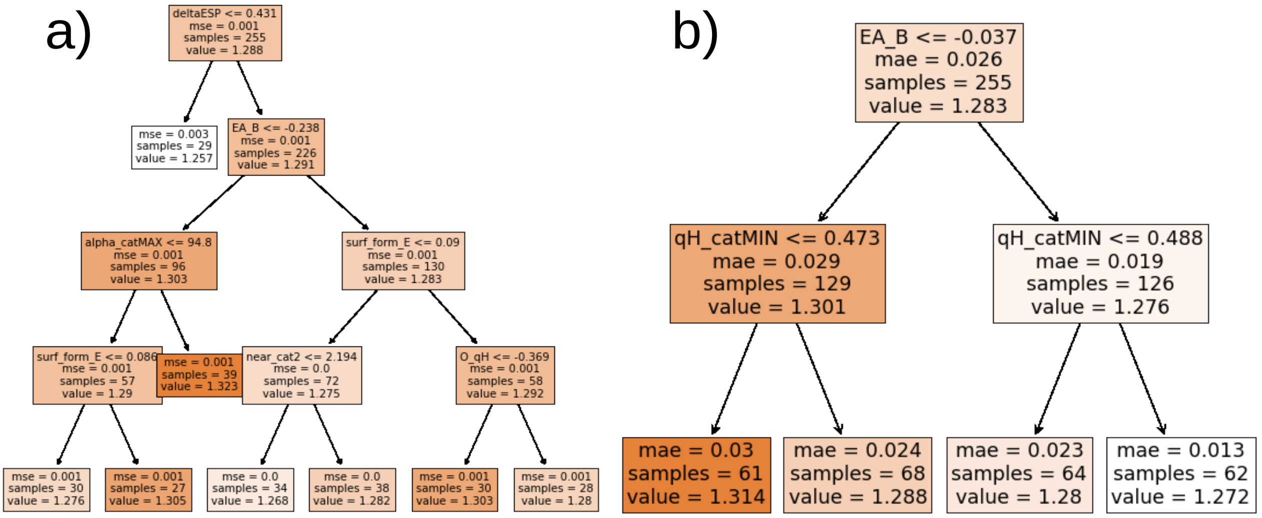

Figure S5. The regression tree models obtained for a) OCO angle as the target with MSE as the cost function; b) OCO angle as the target with MAE as the cost function.

The DTR patterns with the largest mean value are dependent on which cost function is used. With MSE as cost function, the pattern with large *l*(C-O) values is defined as (EA_{max} ≤ -0.24 eV)

AND (α_{max} > 94.80) AND ($\Delta\varphi$ > 0.43 eV), with 39 samples and 1.323 Å average; with MAE, the corresponding pattern is defined as ($EA_{max} \leq$ -0.037 eV) AND ($q_{min} \leq 0.47$ e), with 61 samples and 1.308 Å average. Both patterns significantly exceed the size of the l(C-O) > 1.30 Å subgroups and contain many samples in common. Among samples not present in both patterns, the pattern obtained with MSE has all adsorption sites on La_2O_3, and the pattern from MAE cost function has sites on Na_2O. Both lanthanum and sodium oxide are materials prone to extremely strong carbonation (Table 2). Moreover, the pattern obtained with MAE cost function contains two sites above which CO_2 prefers to physisorb, with l(C-O) = 1.17 Å. This clearly demonstrates the tendency of DTR to overemphasize the importance of data points based solely on the value of target property. DTR minimizes the overall cost function, so that the local regularities are not explicitly considered and are smeared out for the sake of optimizing the global fit, whereas the SGD with quality function (2) is exactly focused on revealing such local subsets. As a result, materials with sites where C-O bond is strongly elongated due to a large charge transfer and the sites above which CO_2 is not activated are selected by DTR together with materials providing moderate charge transfer, but at the same time additional bonding of O atom in adsorbed CO_2 with a surface cation, which also leads to C-O bond elongation. Thus, DTR in this case fails to distinguish these two very different activation modes and, in some cases, cannot even distinguish activation from non-activation.

Other considered indicators of CO_2 activation

1. Dipole moment of the slab induced by adsorbed CO_2 molecule.

The dipole moment of the slab with adsorbed CO_2 molecule indicates both the bending of the molecule and the amount of charge transferred to the molecule upon adsorption (the dipole moment of the slab before adsorption is zero, since we use symmetrically terminated slabs), and thus it indicates the molecule activation. Since in our models the CO_2 adsorption was considered on one side of a surface slab, the dipole moment can be calculated as the difference of electrostatic potentials in vacuum at the two sides of the slab normalized per the surface area. The distribution of the calculated dipole moments in our data shows that certain number of samples has a positive dipole moment (Fig. S6, left), which is the result of surface relaxation upon CO_2 adsorption. We have performed SGD with the minimization of the dipole moment (eq. 1 of the main text), which corresponds to a larger amount of electron density transferred to the CO_2 molecule. Three thresholds have been chosen – -0.002, -0.005, and -0.008. For the cases with both Sabatier principle constrain and without it obtained subgroups are shown in Table S6.

Table S6. The subgroups obtained for SGD minimization of a dipole moment.

threshold	size	subgroup

Dipole minimization without Sabatier principle constraint		
-0.002	57	$d_1 \leq 2.2025$, $d_3 \leq 2.9045$, $U \geq -6.108$, $r_{+1}^{max} \leq 2.8315$
-0.005	23	$L_{min} > -2.19$, $EA_{max} \geq -0.464$, $Q_5 \leq 0.8113$, $Q_6 \leq 0.7756$, $r_{-1}^{max} \leq 1.652$
-0.008	5	$L_{min} > -2.538$, $EA_{max} \leq 0.157$, $d_1 < 1.8635$, $d_2 < 2.037$, $r_{+1}^{min} \leq 2.093$
Dipole minimization with Sabatier principle constraint		
-0.002	46	$CBM \geq -5.1675$, $q_O \geq -0.3906$, $Q_5 \geq 0.51525$, $VBM \leq -5.7975$, $M \geq -7.285$, $q_{max} \leq 0.64775$, $r_{HOMO}^{min} \geq 0.581$
-0.005	12	$L_{min} > -2.19$, $EN_{min} \leq -3.275$, $r_{+1}^{min} \leq 2.807$, $wid \geq 1.242$
-0.008	8	$\varphi_{2.6} \leq 0.66395$, $IP_{min} \leq -5.831$, $c_{min} > -9.361$, $kurt \leq 8.576$, $q_{min} < 0.43575$

The distribution of adsorption energies for obtained subgroups is shown in Fig. S6 left. In all cases where no Sabatier principle constraint was introduced in the quality function there are samples for which strong carbonation is observed with adsorption energies around -3 eV.

Among subgroups obtained with Sabatier principle constraint the one with -0.002 threshold is mostly populated (Table S6). It contains adsorption sites on several mentioned in the main text good catalysts – $LaAlO_3$, Ga_2O_3, but also on a less promising $YInO_3$. Regarding other materials from this subgroup there is no reliable information.

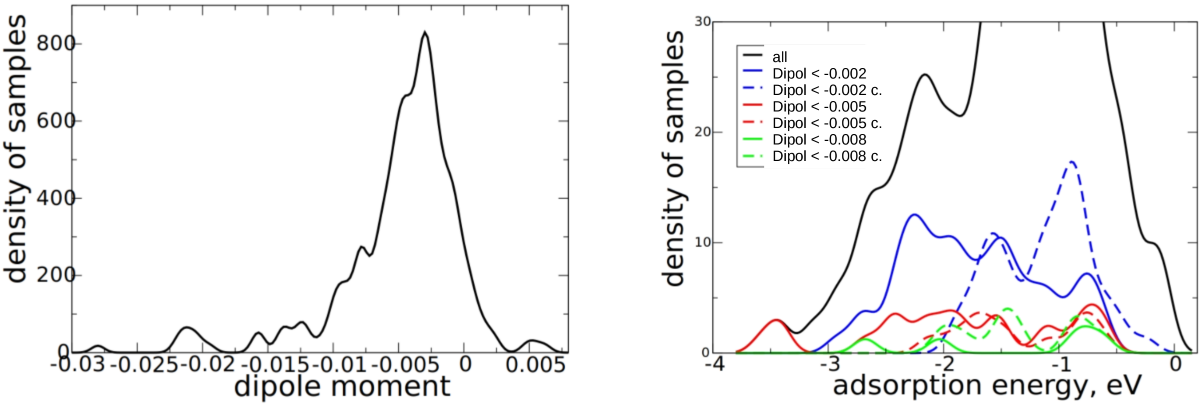

Figure S6. (left) The distribution of samples according to the calculated dipole moment in the whole data set. (right) The distribution of adsorption energies in obtained subgroups.

2. Hirshfeld charge of an adsorbed CO_2.

The physical reasoning behind this indicator is the same as in the case of the dipole moment. Although partitioning of electron density among atoms in a solid is not uniquely defined, different partitioning schemes and in particular Hirshfeld partitioning[18] qualitatively capture changes in electron distribution. SGD was performed with quality function shown in eq. 1 of the main text.

Three thresholds were considered – -0.1, -0.2 and -0.3 *e*. Obtained SGD subgroups are shown in Table S6.

Table S6. The subgroups obtained for SGD minimization of adsorbed CO_2 Hirshfeld charge – $q(CO_2)$.

threshold	size	subgroup
$q(CO_2)$ minimization without Sabatier principle constraint		
-0.1	171	q_O≤-0.3386, Q_6≤0.9458, Δ≤4.07
-0.2	72	$\varphi_{1.4}$≥1.051, Q_5≤0.82885, E_{form}<0.077
-0.3	22	IP_{min}<-6.4695, IP_{max}≥-5.941, q_O<-0.371, d_2≥2.037, r_{+1}^{min}≤2.093
$q(CO_2)$ minimization with Sabatier principle constraint		
-0.1	82	IP_{max}≥-5.941, *VBM*≤-5.0995, Δφ≥0.7326, r_{-1}^{min}≤1.652, α_O≤3.11045
-0.2	39	EA_{max}≤0.005, EA_{max}≥-0.4945, Δφ≥0.7326, r_{-1}^{min}≤1.666, E_{form}≤0.085
-0.3	15	C_6^{min}>485.0, c_{min}≤-9.58, *kurt*≥3.1545, E_{form}<0.062

The distribution of adsorption energies for corresponding subgroups is presented in Fig. S7. For the unconstrained case there is again a domain of samples with large absolute values of adsorption energies. All subgroups obtained with and without Sabatier principle constraint overlap significantly with reduced OCO subgroups. For example the overlap between unconstrained OCO < 132° and $q(CO_2) < 0.1$ *e* subgroups is 91% and 74% of the population respectively, and for corresponding Sabatier principle constrained subgroups – 69 % and 49%.

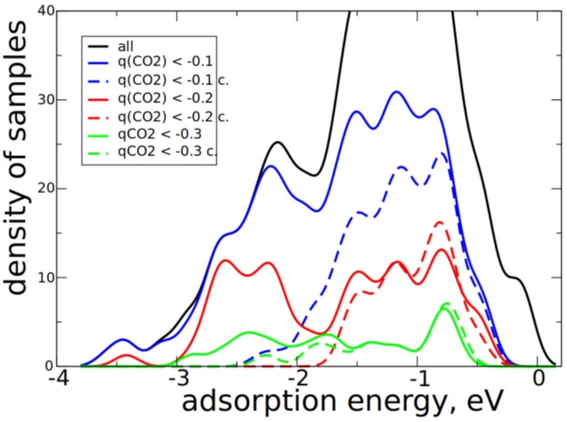

Figure S7. The distribution of adsorption energies in the subgroups of samples with larger absolute values of Hirshfeld charge of an adsorbed CO_2.

3. Difference in Hirshfeld charges of C and O atoms in an adsorbed CO_2

This property indicates the ionicity of a C-O bond. Larger ionicity is expected to correlate with the reactivity in reactions with electrophilic or nucleophilic agents. The calculated CO_2 gas-phase value of the charge difference is 0.44 *e*. It lies within the range of the data for adsorbed CO_2, namely, 0.38-0.52 *e* (Fig. S8, left). We have done the SGD search of subgroups with positive shift with three cutoffs: 0.45, 0.47, and 0.48 *e*. Obtained subgroups are shown in Table S7.

In the case when no Sabatier principle constraint was accounted for, all subgroups contain the samples for which strong carbonation is observed (Fig. S8). There is a certain overlap with reduced OCO subgroups. For example, the subgroup q(C)-q(O) > 0.45*e* contains 18 common samples (49%) with OCO < 130° subgroups. The subgroups obtained with Sabatier principle constraint also partially overlap with constrained OCO subgroups – 10 common samples for q(C)-q(O) > 0.45*e* with OCO > 128° and 16 with OCO > 130° subgroups. Even larger relative overlap is obtained with l(C-O) > 1.30 Å subgroup – 16 samples (67%). Smaller size constrained subgroups with 0.47 and 0.48*e* cutoffs have also about 60% common samples with l(C-O) > 1.30 Å subgroup.

Table S7. The subgroups obtained for SGD maximization of the difference in Hirshfeld charges of C and O atoms.

threshold	size	subgroup
$q(CO_2)$ minimization without Sabatier principle constraint		
0.45	37	W<5.5255, PC>-7.53, C_6<=11.1305, skew>=-2.1615
0.47	9	L_{max}>-1.2615, $\varphi_{1.4}$>=1.2116, α_O<-0.1558
0.48	8	$\Delta\varphi$>=0.996, M>-5.1865, q_{max}>=0.5483
$q(CO_2)$ minimization with Sabatier principle constraint		
0.45	24	EN_{min}<=3.633, EN_{max}>-3.039, PC>=-8.895, r_{HOMO}^{min}<=1.337
0.47	7	C_6^{max}>1440.5, C_6^{min}<=830.5, Q_5<=0.7952, d_2>2.217, r_{HOMO}^{max}>=1.344
0.48	7	C_6^{max}>1440.5, C_6^{min}<=830.5, Q_5<=0.7952, d_2>2.217, r_{HOMO}^{max}>=1.344

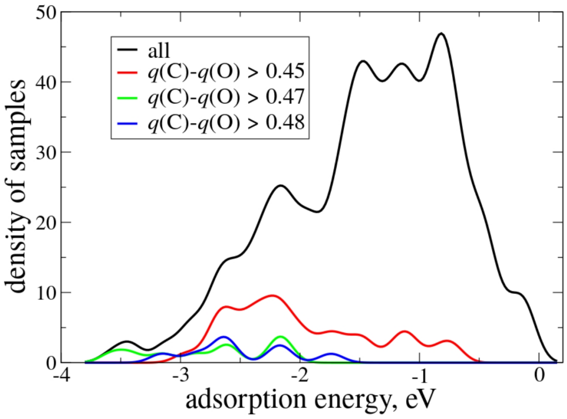

Figure S8. The distribution of adsorption energies in the subgroups with increased *q*(C)-*q*(O) without Sabatier principle constraint.

4. Difference of Hirshfeld charges on O-atoms of an adsorbed CO_2.

As we show, the elongated C-O bonds are observed when the CO_2 molecule is adsorbed in an asymmetric position, so that one oxygen atom is bonded with a surface cation and the other one is protruding. In these cases, the two O-atoms have nonequivalent chemical surroundings. Correspondingly, the difference of Hirshfeld charges on CO_2 oxygens, Δ*q*(O), is expected to indicate this asymmetry. The SGD with the absolute Δ*q*(O) as target property was performed with maximizing this difference with the quality function (1) in the main text. The next thresholds have been considered: 0.01, 0.02 and 0.03 *e*. Obtained subgroups are summarized in Table S8.

The analysis of their populations shows significant overlap with the subgroups for elongated C-O bond distances. For instance, there are 21 common samples in *l*(C-O) > 1.3 Å subgroup and the subgroup with Δ*q*(O) > 0.01 *e*, 81% and 78% of respective populations. The overlap for constrained and unconstrained with Sabatier principle subgroups is 100%. The samples in Δ*q*(O) subgroups with larger thresholds are mostly the same as ones in Δ*q*(O) > 0.01 *e* subgroup. So, we conclude that the difference of Hirshfeld charges on CO_2 oxygen atoms basically reproduces the C-O bond length indicator.

Table S8. The subgroups obtained for SGD maximization of Hirshfeld charges difference on O-atoms in an adsorbed CO_2.

threshold	size	subgroup
maximization of Δ*q*(O) without Sabatier principle constraint		
0.01	25	$\Delta\varphi$>=0.596, *PC*<=-7.207, d_2>2.217, r_{-1}^{min}<=1.1235

maximization of Δq(O) with Sabatier principle constraint		
0.01	26	EA_{max}<=0.005, c_{min}<=-5.849, d_2>2.217, q_{min}<=0.51
0.02	19	C_6^{max}>=580.5, EA_{max}<=0.0375, $\varphi_{1.4}$>=0.66415, IP_{min}<=6.4695, α_{max}>90.75, C_6>=9.025
0.03	11	IP_{max}>-5.5225, α_{min}<=60.55, d_1<=1.9585, M>=-7.555, α_O>=0.2268

References

1. Blum, V. et al. Ab initio molecular simulations with numeric atom-centered orbitals. *Comput. Phys. Comm.* **180**, 2175-2196 (2009).
2. Perdew, J. P., Burke, K. & Ernzerhof, M. Generalized gradient approximation made simple. *Phys. Rev. Lett.* **77**, 3865–3868 (1997).
3. Perdew, J. P. et al. Restoring the density-gradient expansion for exchange in solids and surfaces. *Phys. Rev. Lett.* **100**, 136406 (2008).
4. Tkatchenko, A. & Scheffler, M. Accurate molecular van der Waals interactions from ground-state electron density and free-atom reference data. *Phys. Rev. Lett.* **102**, 073005 (2009).
5. Ceperley, D. M. & Alder, B. J. Ground state of the electron gas by a stochastic method. *Phys. Rev. Lett*. **45**, 566–569 (1980).
6. Hammer, B., Hansen, L. B. & Nørskov, J. K. Improved adsorption energetics within density-functional theory using revised Perdew-Burke-Ernzerhof functionals. *Phys. Rev. B* **59**, 7413-7421 (1999).
7. Blaylock, D. W., Ogura, T., Green, W. H. & Beran, G. J. O. Computational investigation of thermochemistry and kinetics of steam methane reforming on Ni(111) under realistic conditions. *J. Phys. Chem. C* **113**, 4898-4908 (2009).
8. Peterson, A. A., Abild-Pedersen, F., Studt, F., Rossmeisl, J., Nørskov, J. K. How copper catalyzes the electroreduction of carbon dioxide into hydrocarbon fuels. *Energy Environ. Sci.* **3**, 1311-1315 (2010).
9. Neugebauer, J. & Scheffler, M. Adsorbate-substrate and adsorbate-adsorbate interactions of Na and K adlayers on Al(111). *Phys. Rev. B.* **46**, 16067-16080 (1992).
10. Solis, B. H. et al. Initial stages of CO_2 adsorption on CaO: a combined experimental and computational study. *Phys. Chem. Chem. Phys.* **19**, 4231-4242 (2017).
11. Wang, Y. et al. CO_2 activation by ZnO through the formation of an unusual tridentate surface carbonate. *Angew. Chem. Int. Ed.* **46**, 5624–5627 (2007).
12. Xia, X., Strunk, J., Busser, W., Naumann d'Alnoncourt, R., Muhler, M. Probing the surface heterogeneity of polycrystalline zinc oxide by static adsorption microcalorimetry. 1. The influence of the thermal pretreatment on the adsorption of carbon dioxide. *J. Phys. Chem. C* **112**, 10938–10942 (2008).
13. Bučko, T., Lebegue, S., Angyan, J. G. & Hafner, J. Extending the applicability of the Tkatchenko-Scheffler dispersion correction via iterative Hirshfeld partitioning. *J. Chem. Phys.* **141**, 034114 (2014).
14. Meixner, D., Arthur, D., George, S. Kinetics of desorption, adsorption, and surface diffusion of CO_2 on MgO(100). *Surf. Sci. 261*, 141–154 (1992).
15. Mazheika, A. & Levchenko, S. V. Ni Substitutional Defects in bulk and at the (001) surface of MgO from first-principles calculations. *J. Phys. Chem. C* **120**, 26934–26944 (2016).
16. http://nomad-repository.eu/
17. Hinuma, Y., Hayashi, H., Kumagai, Y., Tanaka, I., Oba, F. *Phys. Rev. B* **96**, 094102 (2017).
18. Hirshfeld, F. L. Bonded-atom fragments for describing molecular charge densities. *Theor. Chim. Acta*, **44**, 129–138 (1977).